

Tunable two-dimensional superlattices in graphene

Robin Huber,¹ Ming-Hao Liu,^{2,*} Szu-Chao Chen,² Martin Drienovsky,¹ Andreas Sandner,¹ Kenji Watanabe,³ Takashi Taniguchi,³ Klaus Richter,⁴ Dieter Weiss,¹ and Jonathan Eroms^{1,†}

¹*Institute of Experimental and Applied Physics, University of Regensburg, D-93040 Regensburg, Germany*

²*Department of Physics, National Cheng Kung University, Tainan 70101, Taiwan*

³*National Institute for Materials Science, 1-1 Namiki, Tsukuba 305-0044, Japan*

⁴*Institute of Theoretical Physics, University of Regensburg, D-93040 Regensburg, Germany*

(Dated: June 18, 2022)

Electrons in an artificially created periodic potential—a superlattice—follow Bloch’s theorem, and they reside in minibands^{1,2}. This approach is particularly suitable to study effects inaccessible in natural crystals, such as Hofstadter’s butterfly³. After pioneering experiments using high-mobility GaAs based superlattices,^{4,5} additional proof^{6–8} came with graphene-hexagonal boron nitride (hBN) heterostructures^{9,10} forming moiré superlattices. However, both lattice symmetry and period are constrained by the crystal lattices of graphene and hBN, and the exact potential^{11,12} is governed by, *e.g.*, strain or local band-gaps, which are virtually impossible to be controlled experimentally. A first approach to circumvent this was recently presented by Forsythe *et al.*, who employed a patterned dielectric, and demonstrated gate-tunable superlattice effects.¹³ In this work, combining patterned and uniform gates,^{14,15} we demonstrate satellite resistance peaks corresponding to Dirac cones to fourth order, and the Hofstadter butterfly, including the non-monotonic quantum Hall response predicted by Thouless *et al.*¹⁶. The exact potential shape can be determined from elementary electrostatics¹⁷, allowing for a detailed comparison between miniband structure and calculated transport characteristics. We thus present a comprehensive picture of graphene-based superlattices, featuring a broad range of miniband effects, both in experiment and in our theoretical modeling.

Electrons subjected to both a periodic potential and a uniform, perpendicular magnetic field exhibit a fractal band structure governed by the ratio of magnetic flux ϕ per lattice unit cell and the magnetic flux quantum $\phi_0 = h/e$. For weak magnetic field and strong lattice potential, Hofstadter first calculated the band structure, which shows continuous bands for rational $\phi/\phi_0 = p/q$ with p and q co-prime integers and exhibit a self-similar structure, which was coined Hofstadter butterfly due to its peculiar shape.³ For the opposite case of strong magnetic field and weak lattice potential, the band structure is controlled by the inverse flux $\phi_0/\phi = q/p$ instead¹⁸. As was first shown by Thouless *et al.* the transverse resistance is quantised, whenever the Fermi level lies within a gap, either in between Landau levels, or within the Hofstadter spectrum¹⁶. This observation formed the theoretical basis for understanding the precise quantisation of the quantum Hall plateaus, using notions of topology^{19,20}. For a system where the Hofstadter spectrum is present, the filling factor ν and quantum Hall plateau values are linked by a Diophantine equation,^{16,18,21}

$$\nu = (\phi_0/\phi)s + t, \quad (1)$$

where s and t are integers such that $R_{xy} = \frac{h}{t e^2}$. Note that $s = 0$ represents the standard quantum Hall physics ($\nu = t$), and values $s \neq 0$ are associated with internal gaps of the Hofstadter butterfly. In the latter case, the transverse quantum Hall resistance does not follow the filling factor ν in a monotonic way¹⁶. Since in the recursive Hofstadter spectrum there are infinitely many gaps, the transverse

resistance will show more and more non-monotonic steps, as an increasing number of gaps is resolved in experiment.

First efforts to detect this band structure were performed in high-mobility GaAs-based two-dimensional (2D) electron gases^{4,5}, showing minigaps, and also non-monotonic Hall curves. However, the lattice period was limited to $a \geq 100$ nm due to technological constraints. Utilizing moiré lattices formed in graphene/hBN heterostructures^{22,23}, the Hofstadter butterfly was unambiguously demonstrated^{6–8}. However, the maximum lattice period in this case is limited to about 14 nm, given by the lattice mismatch between hBN and graphene. This means that the condition of one magnetic flux quantum per unit cell area requires at least 25 T, out of scope for standard laboratory magnets. In addition, the lattice symmetry is determined to be hexagonal, and the potential is not gate-tunable. Finally, even though a complete theoretical description of moiré lattices was presented^{11,12}, many terms including strain or local gaps have to be included, which are poorly controlled experimentally. 2D superlattices in graphene were also realized in etched graphene antidot lattices²⁴, showing ballistic transport^{25–28} and superlattice Dirac points^{29,30}, but due to the strong potential, which cannot be tuned, more subtle effects are not visible. Therefore, a more flexible method with a gate-defined superlattice potential is required. A first approach was pursued by Forsythe *et al.*, based on a patterned dielectric¹³. Here, both square and hexagonal lattices were realised, resulting in satellite Dirac peaks²⁹ and observation of

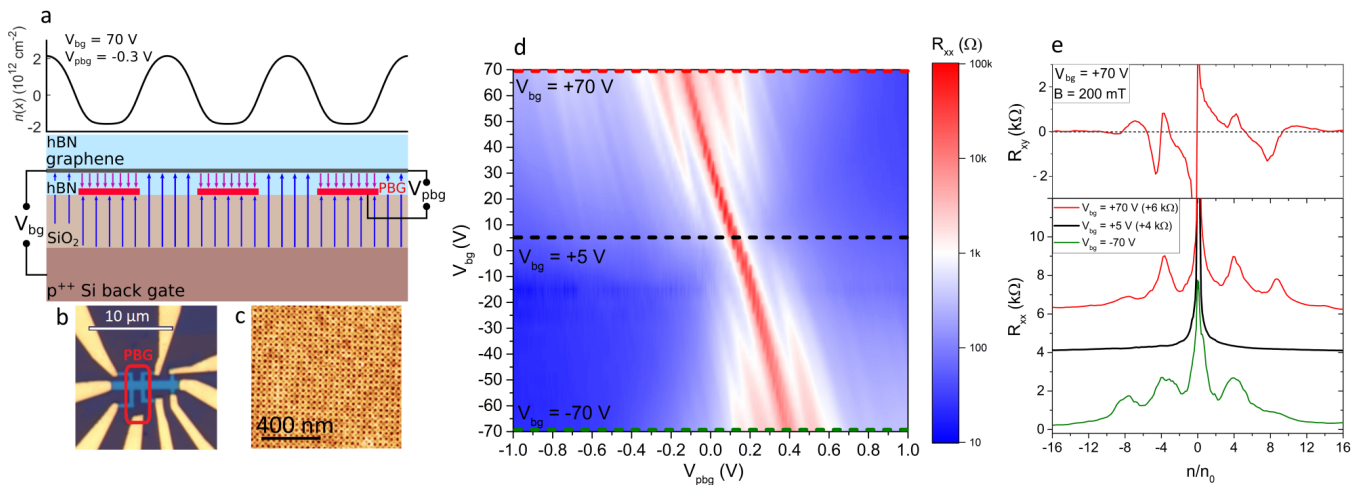


FIG. 1. **Sample Layout and Gate Response at Zero Magnetic Field.** **a** Schematic of the sample geometry. Due to the interplay between a Si backgate and a few-layer graphene patterned bottom gate (PBG), a periodic charge carrier density modulation can be induced in the encapsulated graphene layer on top of the two gates. **b** Micrograph of the studied device in Hall bar geometry and Cr/Au edge contacts. Red line marking the position of the PBG. **c** AFM picture of the PBG with a square superlattice and a lattice constant of $a = 40$ nm. For the studied sample, a periodic array of holes was etched into a bilayer graphene flake. **d** Gate map of the device at $T = 1.5$ K. Longitudinal resistance R_{xx} as a function of backgate voltage V_{bg} and PBG voltage V_{pbg} . By increasing the backgate voltage, *i.e.*, increasing the modulation strength, satellite peaks start to occur besides the main Dirac peak. **e** Linecuts at three different backgate voltages highlight the additional features upon tuning the periodic potential strength. Upper panel shows the sign change of the corresponding Hall resistance R_{xy} at the position of the satellite Dirac points at $B = 200$ mT.

gaps in the Hofstadter butterfly. However, the non-monotonic transverse resistance, predicted by Thouless, was not observed, requiring further improvements in device quality.³¹

Our samples (see Fig. 1a) consist of a single-layer graphene sheet encapsulated in hBN and placed on top of a few-layer graphene patterned bottom gate (PBG) residing on an oxidised silicon substrate. Importantly, the lower hBN is only 5 nm thin to prevent damping of the electrostatic potential. In addition, the doped Si serves as a uniform backgate. More details are given in the Methods section and previous reports^{14,15}. By using this gating scheme, a widely tunable 2D periodic charge carrier density modulation can be induced in the graphene layer ranging from unipolar to bipolar potential profile with tunable potential strength (see Supplementary Information for gate maps of polarity regime, modulation strength and average carrier density). Figure 1b shows a micrograph of the studied device with red outlining the position of the PBG, and in Fig. 1c, an atomic force microscopy (AFM) image of the PBG with a square lattice of period $a = 40$ nm can be seen. Figure 1d shows the gate response of the longitudinal resistivity R_{xx} at $B = 0$ and $T = 1.5$ K. As can clearly be seen, the PBG voltage V_{pbg} largely controls the overall carrier density, and the Si backgate voltage V_{bg} mainly sets the modulation strength. For $V_{bg} \approx 0$ V, only one Dirac peak is visible, as expected for intrinsic graphene. The field effect mobility extracted at low backgate voltage is about $40\,000$ cm²/Vs. By increasing V_{bg} , *i.e.*, in-

creasing the potential strength, several pronounced satellite peaks start to appear next to the main Dirac peak. Figure 1e shows R_{xx} plotted as a function of normalised charge carrier density n/n_0 (with $n_0 = 1/a^2$) which gives the number of electron/holes per superlattice unit cell area for three different backgate voltages $V_{bg} = 5$ V and $V_{bg} = \pm 70$ V. The most pronounced satellite peaks manifest when one superlattice unit cell is filled up with 4 and 8 electrons/holes which reflects the 4-fold degeneracy of graphene. These satellite peaks are accompanied by sign changes of the Hall resistance R_{xy} at a small magnetic field of $B = 200$ mT (see upper panel of Fig. 1e). This confirms that the carrier type changes between electron and hole conduction, and proves the existence of well-defined superlattice-induced minibands. Also, when the sign of the backgate voltage is reversed, the satellite Dirac peaks are mirrored with respect to the main Dirac peak.

To confirm these findings, we have performed quantum transport simulations (based on the Landauer-Büttiker approach) and calculated miniband structures at zero magnetic field, $B = 0$ T, both employing the realistic square superlattice potential obtained from finite-element-based electrostatic simulation taking into account the geometry of our device; see Methods. Fig. 2a shows the simulated longitudinal resistance R_{xx} as a function of V_{pbg} at fixed $V_{bg} = 58$ V for a six-terminal Hall bar (left inset of Fig. 2b). Several R_{xx} peaks can be observed, around each of which clear sign changes of the Hall resistance R_{xy} at $B = 200$ mT are visible (see Sup-

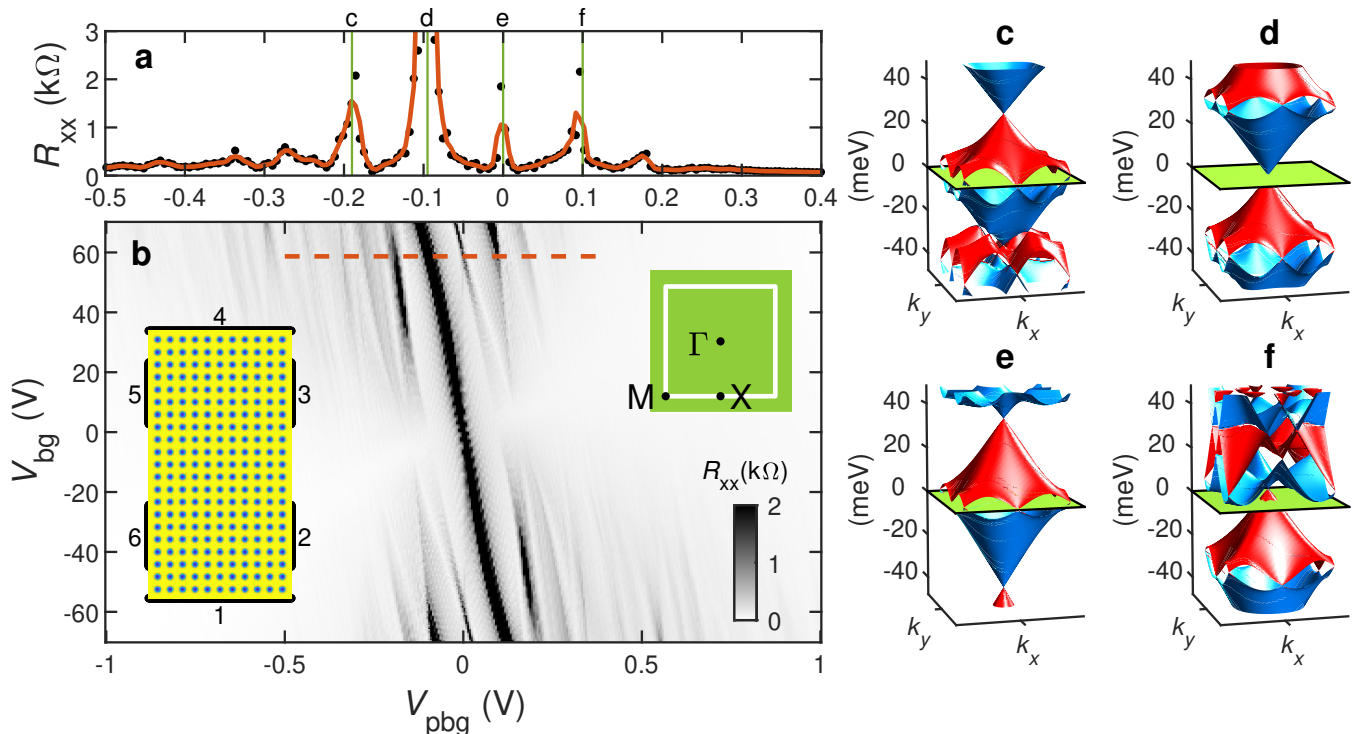


FIG. 2. **Transport Simulation and Band Structure.** **a** Four-terminal longitudinal resistance R_{xx} taken at $V_{bg} = 58$ V (dashed line in **b**). Continuous line shows smoothed data, and the black dots are the raw simulation results. Marked positions correspond to band structure plots. **b** Gate map of R_{xx} at zero magnetic field. Left inset: Geometry of the simulation. Right inset: Mini-Brillouin zone of the square superlattice with points of high symmetry. **c** to **f**: Band structure plots at positions marked in **a**. In each diagram, the green plane shows the position of the Fermi level.

plementary Information). Specifically, two R_{xx} satellite Dirac peaks to the right of the main Dirac point and one to the left can clearly be seen in Fig. 2a, similar to the experimental data taken at large positive backgate voltage. This order reverses for large negative V_{bg} , as seen in the simulated R_{xx} map as a function of V_{pbg} and V_{bg} shown in Fig. 2b. Similar to Fig. 1d from the experiment, the resistance map of Fig. 2b shows a strong main Dirac peak throughout all backgate voltages, accompanied by a few faint lines parallel to the main Dirac line emerging with increasing $|V_{bg}|$. A comparison with Fig. 1d shows an excellent agreement between our experiment and simulation.

The origins of the resistance peaks shown in Figs. 2a and b can be identified by comparing with our miniband structure calculations. A few examples are shown in Fig. 2c-f, where we have fixed the Fermi energy at zero represented by the green plane. The main Dirac peak is observed when the Fermi level lies exactly at the Dirac point of the unperturbed graphene band structure (d). The first satellite peak (c and e for hole and electron side) corresponds to well-resolved secondary and tertiary Dirac cones at the X and M points of the (square) mini-Brillouin zone (right inset on Fig. 2b), while the second satellite resistance peak (f) is found when a large Dirac cone reappears at the center of the mini-Brillouin zone.

It is somewhat obscured by higher bands intersecting the Fermi level. We provide a full movie of the miniband structures as V_{pbg} is swept through the line trace of the resistance in the Supplementary Information. In addition to the features highlighted in Fig. 2, the movie shows that additional peaks are progressively harder to resolve as many minibands of electron and hole character are present at the Fermi level.

Now we focus on the high-field regime, where the Hofstadter energy spectrum is expected. In order to experimentally observe signatures of this energy spectrum the magnetic flux ϕ per superlattice unit cell area has to be of the order of one magnetic flux quantum ϕ_0 . For the studied sample with a square superlattice of nominal lattice constant $a = 40$ nm, $\phi/\phi_0 = 1$ is reached experimentally at a magnetic field of $B = 2.7$ T (corresponding to an actual lattice period of $a = 39$ nm). Figure 3a shows the longitudinal resistance as a function of normalised charge carrier density n/n_0 and magnetic fields up to 9 T. The magnetotransport data show additional features besides the main Landau fan, which emerge from the newly created satellite Dirac peaks as shown in Fig. 3a. At higher fields the main Landau fan exhibits additional minima in longitudinal resistance which cannot be traced back to the original Dirac point and correspond to superlattice induced energy gaps.

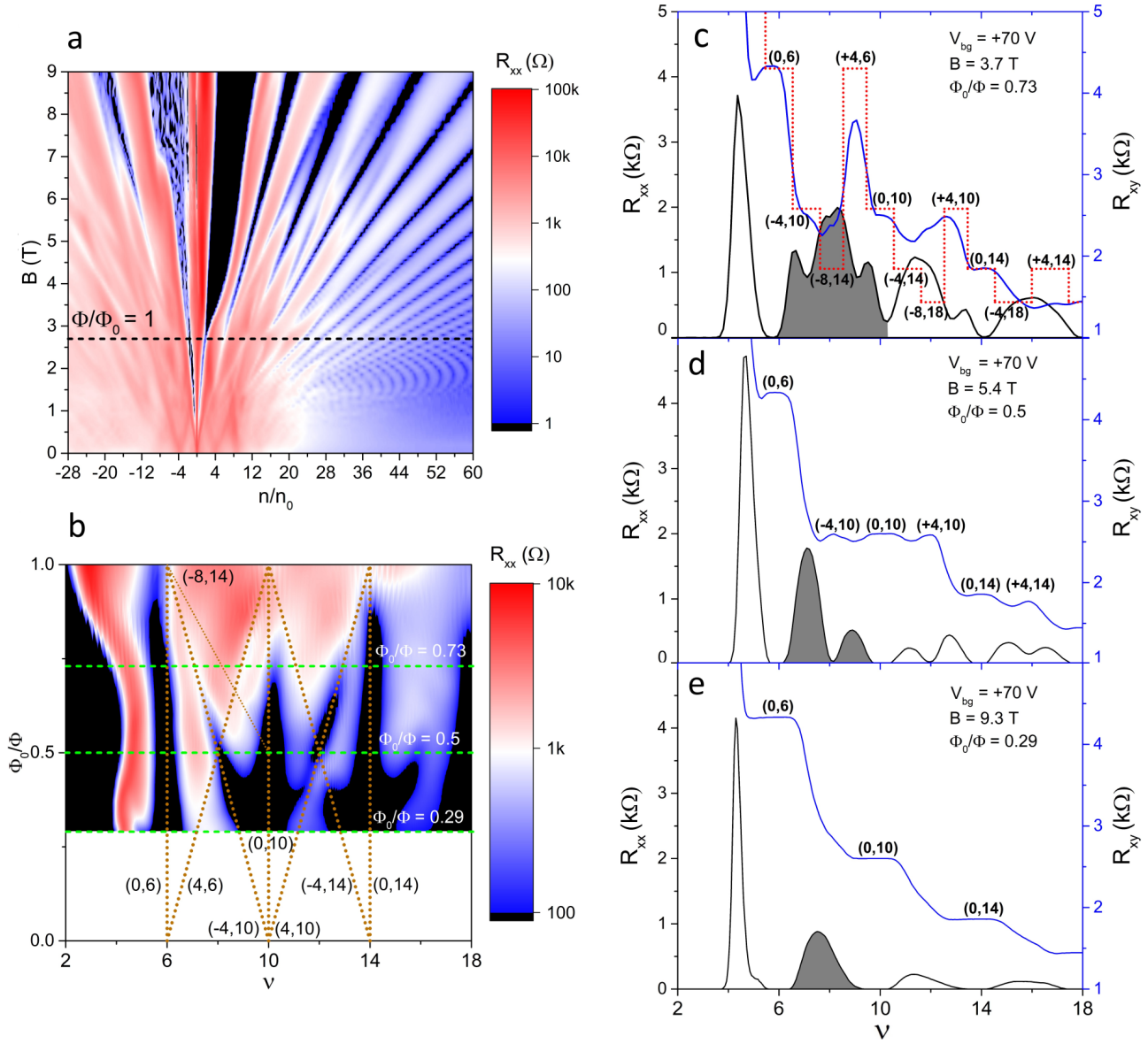


FIG. 3. **Experimental Magnetotransport Data at Large Fields.** **a** R_{xx} plotted as a function of magnetic field and normalised charge carrier density n/n_0 . Landau fans emerge from the main Dirac point and satellite Dirac points giving rise to superlattice induced energy gaps manifesting as additional minima in longitudinal resistance. The data were taken at $T = 1.5$ K and a backgate voltage of $V_{bg} = 70$ V. **b** Replot of the data in **a** in a Wannier diagram with Landau level filling factor ν and inverse flux ϕ_0/ϕ . Vertical minima correspond to energy gaps between Landau levels, additional diagonal features are signatures of the largest energy gaps of the Hofstadter butterfly energy spectrum. Dotted lines highlight the Landau gaps (vertical) and Hofstadter gaps (diagonal). **c** to **e** show linecuts at certain magnetic fields from the data in **b** showing the evolution of the magnetic bandstructure upon changing the magnetic flux per superlattice unit cell area. Energy gaps in the spectrum correspond to minima in R_{xx} and plateaus in R_{xy} and follow the equation $\nu = (\phi_0/\phi)s + t$. The observed energy gaps are labeled by their parameters (s, t) . Features with $s \neq 0$ correspond to superlattice induced energy gaps. The dotted red line in **c** shows the ideal non-monotonic quantum Hall sequence evaluated for s between -8 and 4 .

To resolve the Hofstadter features better, in Fig. 3b we replot part of the data in a Wannier diagram, *i.e.* the inverse flux ϕ_0/ϕ versus the filling factor ν . In this diagram, features belonging to quantum Hall states of the unpatterned graphene ($s = 0$, $\nu = 2, 6, 10, \dots$) appear as vertical lines while the energy gaps of the Hofstadter

spectrum ($s \neq 0$) form diagonal lines. The largest energy gaps ($s = \pm 4$) are clearly resolved, following Eq. (1).

The evolution of the magnetic band structure as a function of magnetic field becomes apparent by looking at the longitudinal and transverse resistance at certain values of magnetic flux per superlattice unit cell area

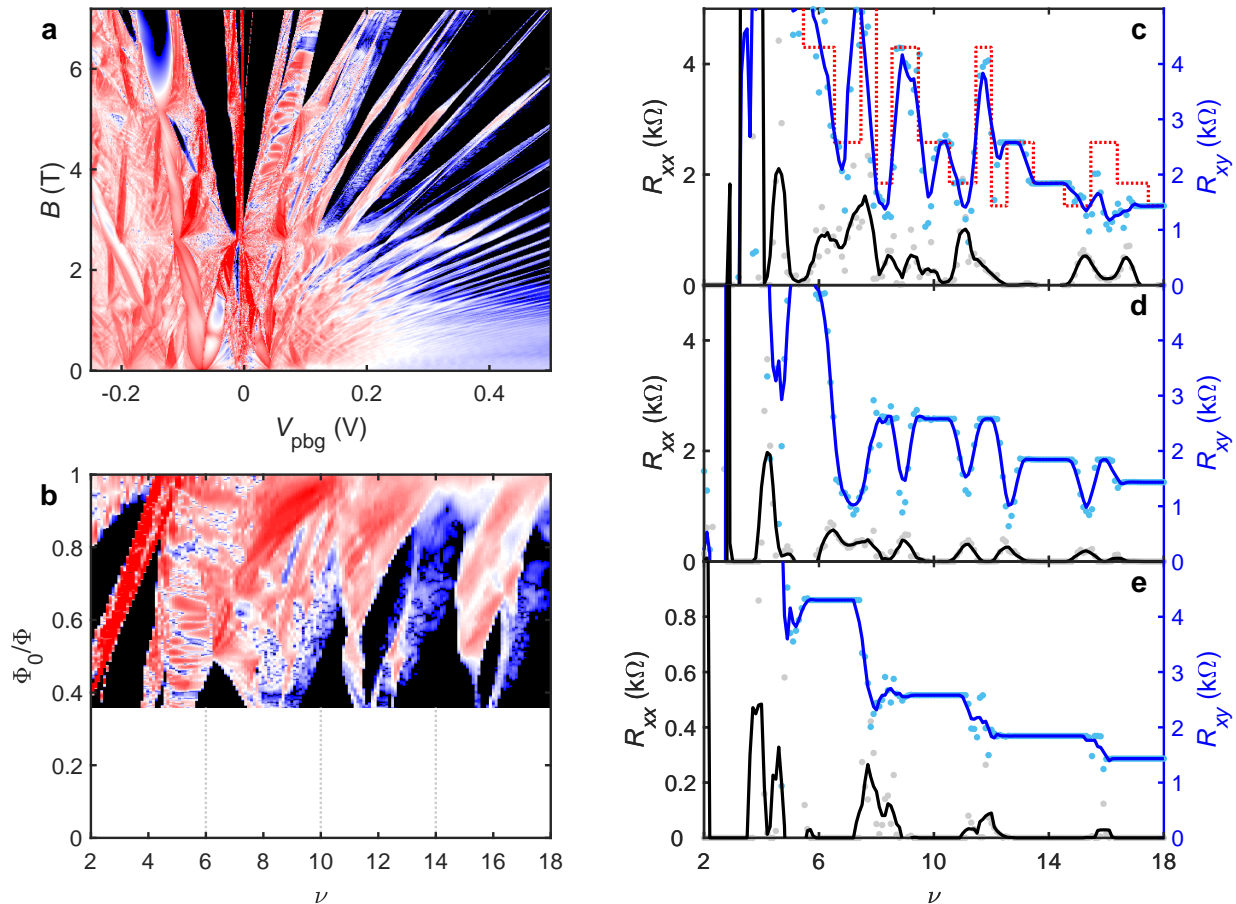


FIG. 4. **Simulated Transport at Large Fields.** Each panel corresponds to a similar panel in Fig. 3. **a** Landau fan plot of R_{xx} on a log scale at a fixed back gate voltage of $V_{bg} = 50$ V. **b** Wannier diagram of R_{xx} . **c-e** line cuts of the Hall (blue) and longitudinal resistance (black) at $\phi_0/\phi = 0.73$, 0.50, and 0.36. Lines were smoothed over 5 neighbouring data points, raw data are shown as round dots. In panel **c**, the dotted red line shows the predicted positions for the quantum Hall plateaus, evaluated for s between -8 and $+8$.

(dashed horizontal lines in Fig. 3b). At high magnetic fields ($\phi_0/\phi = 0.29$), the usual sequence of quantum Hall plateaus can be observed, as expected for intrinsic monolayer graphene (see Fig. 3e). By changing the magnetic flux ratio to $\phi_0/\phi = 0.5$ a splitting of Landau bands into two minibands occurs. Additional minima in R_{xx} can be observed accompanied by well developed quantum Hall plateaus (see Fig. 3d). At a magnetic flux ratio of $\phi_0/\phi = 0.73$ the quantum Hall resistance shows signatures of the two largest gaps ($s = \pm 4$) of the Hofstadter butterfly (see Fig. 3c). This is best visible in the second Landau band between $\nu = 6$ and $\nu = 10$ where R_{xx} exhibits two additional minima, and the corresponding quantum Hall resistance R_{xy} exhibits a non-trivial, non-monotonic sequence following the expected sequence of quantum Hall values if the Fermi energy is shifted into the largest energy gaps in the Hofstadter spectrum.¹⁶ In addition there is also a tendency to approach the plateau value associated with $s = -8$, *i.e.* the next iteration of

the self-similar spectrum. These findings confirm the prediction by Thouless *et al.*¹⁶ in a gate-defined superlattice in graphene.

The situation at high magnetic fields was also modeled in transport calculations. Due to the restriction of the implemented scaled tight-binding approach³² (see Methods), we consider a magnetic field range of up to $B = 7.2$ T, which corresponds to $\phi_0/\phi = 0.36$. For determining the electrostatic potential, we excluded the carrier density correction due to quantum capacitance, as there is no closed-form expression due to the graphene density of states deformed by finite magnetic field, contrary to the case at $B = 0$. Therefore, the capacitance of both gates only contains the geometric capacitance resulting in a larger gate coupling. Nevertheless, by calculating the positions where the superlattice unit cells are filled with a multiple of four electrons or holes, we can match the features in the calculated Landau fan diagram with the experimental ones. This is done in Fig. 4, where each

panel of the experimental Fig. 3 matches a corresponding panel in the theory Fig. 4. All data were calculated for $V_{bg} = 50$ V. The similarity is quite striking. The Landau fan diagram (Fig. 4a) shows Landau levels emanating from the main and the satellite Dirac peaks. For negative V_{pbg} (bipolar regime, opposite to V_{bg}), resistance values are higher, while on the positive V_{pbg} side, overall resistances are lower, and the energy gaps are better resolved. Additional simulation data at $V_{bg} = 70$ V are shown in the Supplementary Information. To obtain the Wannier diagram in Fig. 4b, we calculated the filling factor by taking straight lines from the main Dirac peak at $V_{pbg} = -0.065$ V to the largest energy gaps at high field and density and interpolated from the raw data. We note that close to the main Dirac peak, the Landau fan does not form straight lines, but starts out curved. The reason for this is unknown, but we speculate that in this region the carrier density in each unit cell is strongly non-uniform, leading to a deviation from the standard definition of the filling factor. Therefore, the disentangling of Landau and Hofstadter gaps for the calculated data is not as clear-cut as for the experimental data. Still we observe dark regions (low resistance) both for standard filling factors $\nu = 6, 10, 14, 18$ and additional Hofstadter gaps. When taking line traces of the Hall resistance at different flux ratios, the calculations reproduce the non-monotonic behavior of R_{xy} . For all flux ratios shown, we find a strong correspondence between experimental and numerical data. The peak splitting in R_{xx} is also reproduced qualitatively, but since the calculations were done without disorder, one cannot expect a one-to-one match.

In conclusion, we have presented an experimental realization of gate-tunable 2D superlattices in graphene with an arbitrary geometry, showing transport signatures of up to quaternary Dirac points, the Hofstadter energy spectrum and the non-trivial, non-monotonic quantum Hall response, all owing to the modified band structure. Transport calculations at $B = 0$ and $B \neq 0$, based on a real-space Green's function method can reproduce the experimental data to high precision and support our interpretation. At $B = 0$, the continuum model considering the same superlattice potential allows us to identify strong resistance features with isolated Dirac cones in the miniband structure, and explains why no further resistance peaks are observed. For large fields we calculate Landau fans corresponding to additional Dirac points, and also reproduce the non-monotonic quantum Hall response in detail. The excellent correspondence between theory and experiment is striking and allows for a complete understanding of the observed transport features. Our experimental approach will also be suitable for studying more advanced geometries, such as the Lieb lattice³³ or symmetric one-dimensional superlattices³⁴, which are not accessible by other methods.

METHODS:

Sample fabrication and data acquisition For the fabrication of the patterned bottom gates (PBG), we use standard electron beam lithography (EBL) and reactive

ion etching with O_2 plasma to pattern few layer graphene flakes with thicknesses between 2 to 5 layers. We apply several cleaning steps after the processing with Remover PG (Microchem) at 60°C and annealing in vacuum at 400°C to remove PMMA and other residues and check the patterned bottom gates by means of AFM. After choosing a clean and suitable PBG we use the van der Waals pick up technique to encapsulate monolayer graphene between two hBN flakes and transfer the graphene/hBN heterostructure onto the PBG. The bottom hBN layer is chosen to be only a few nm thick in order to achieve a well defined potential modulation. In the next step the stack is shaped into Hall bar geometry by EBL and selective reactive ion etching³⁵ with SF_6 and O_2 . Edge contacts are made by EBL and $Cr(5\text{nm})/Au(80\text{nm})$. All transport measurements were conducted in a ^4He cryostat with a base temperature of 1.5 K and standard lock-in techniques at a constant current of 10 nA.

Transport calculations Our transport calculations for four-probe measurements follow the Landauer-Büttiker formalism,³⁶ which requires to calculate all $6 \times 5 = 30$ transmission functions for the considered Hall bar (left inset of Fig. 2b). Each transmission function T_{pq} between lead p and lead q is obtained using the real-space Green's function based on a scaled graphene lattice.^{32,37,38} For Fig. 2 with $B = 0$ and Fig. 4 with strong B , we have chosen scaling factors of $s_f = 8$ and $s_f = 7$, respectively, in order for the scaling criteria³² to be fulfilled. More details are described in Ref. 39. To obtain realistic onsite energy profiles due to the spatially modulated gate capacitances, we first build a three-dimensional electrostatic model to extract gate capacitances of the patterned bottom gate C_{pbg} and the global back gate C_{bg} , using FENICS⁴⁰ (automated partial-differential equation solver) and GMSH⁴¹ (finite-element mesh generator). The classical carrier density is given by $n_{cl} = (C_{pbg}/e)V_{pbg} + (C_{bg}/e)V_{bg}$. For transport calculations at zero magnetic field (Fig. 2), we include the correction Δn due to the quantum capacitance¹⁷ to obtain the net carrier density $n = n_{cl} + \Delta n$; for finite magnetic field (Fig. 4), we approximate the density with n_{cl} for reasons mentioned in the main text. The on-site energy corresponding to the carrier density is related by $V(x, y) = -\text{sgn}[n(x, y)]\hbar v_F \sqrt{\pi|n(x, y)|}$ (v_F the Fermi velocity of electrons in graphene) through the Dirac equation, in order to fix the global Fermi level at zero³² for transport calculations.

AUTHOR CONTRIBUTIONS

R.H., D.W. and J.E. conceived the experiment, R.H., M.D. and A.S. developed the patterned gate preparation, R.H. fabricated the samples under study and performed transport measurements, K.W. and T.T. grew boron nitride crystals, M.-H.L. and K.R. developed the transport theory, M.-H.L. did transport calculations and S.-C.C. performed miniband calculations. R.H., J.E. and M.-H.L. wrote the manuscript with input from all co-authors.

ACKNOWLEDGEMENTS

M.-H.L. and S.-C.C. are supported by Taiwan Ministry of Science (107-2112-M-006-004-MY3 and 107-2627-E-006-001) and Ministry of Education (Higher Education Sprout Project). Growth of hexagonal boron nitride crystals was supported by the MEXT Element Strategy Ini-

tiative to Form Core Research Center, Grant Number JP-MXP0112101001 and the CREST(JPMJCR15F3), JST. This work was supported by the Deutsche Forschungsgemeinschaft (DFG, German Research Foundation) project-id 314695032 SFB 1277 (subprojects A07, A09) and GRK 1570.

- * minghao.liu@phys.ncku.edu.tw
 † jonathan.eroms@ur.de
- ¹ L. V. Keldysh, "Effect of ultrasonics on the electron spectrum of crystals," *Soviet Physics Solid State* **4**, 1658 (1963).
 - ² L. Esaki and R. Tsu, "Superlattice and negative differential conductivity in semiconductors," *IBM Journal of Research and Development* **14**, 61–65 (1970).
 - ³ Douglas R. Hofstadter, "Energy levels and wave functions of bloch electrons in rational and irrational magnetic fields," *Phys. Rev. B* **14**, 2239–2249 (1976).
 - ⁴ C. Albrecht, J. H. Smet, K. von Klitzing, D. Weiss, V. Umansky, and H. Schweizer, "Evidence of hofstadter's fractal energy spectrum in the quantized hall conductance," *Phys. Rev. Lett.* **86**, 147–150 (2001).
 - ⁵ M. C. Geisler, J. H. Smet, V. Umansky, K. von Klitzing, B. Naundorf, R. Ketzmerick, and H. Schweizer, "Detection of a landau band-coupling-induced rearrangement of the hofstadter butterfly," *Phys. Rev. Lett.* **92**, 256801 (2004).
 - ⁶ C. R. Dean, L. Wang, P. Maher, C. Forsythe, F. Ghahari, Y. Gao, J. Katoch, M. Ishigami, P. Moon, M. Koshino, T. Taniguchi, K. Watanabe, K. L. Shepard, J. Hone, and P. Kim, "Hofstadter's butterfly and the fractal quantum hall effect in moire superlattices," *Nature* **497**, 598–602 (2013).
 - ⁷ B. Hunt, J. D. Sanchez-Yamagishi, A. F. Young, M. Yankowitz, B. J. LeRoy, K. Watanabe, T. Taniguchi, P. Moon, M. Koshino, P. Jarillo-Herrero, and R. C. Ashoori, "Massive dirac fermions and hofstadter butterfly in a van der waals heterostructure," *Science* **340**, 1427–1430 (2013).
 - ⁸ L. A. Ponomarenko, R. V. Gorbachev, G. L. Yu, D. C. Elias, R. Jalil, A. A. Patel, A. Mishchenko, A. S. Mayorov, C. R. Woods, J. R. Wallbank, M. Mucha-Kruczynski, B. A. Piot, M. Potemski, I. V. Grigorieva, K. S. Novoselov, F. Guinea, V. I. Fal'ko, and A. K. Geim, "Cloning of dirac fermions in graphene superlattices," *Nature* **497**, 594–597 (2013).
 - ⁹ C. R. Dean, A. F. Young, I. Meric, C. Lee, L. Wang, S. Sorgenfrei, K. Watanabe, T. Taniguchi, P. Kim, K. L. Shepard, and J. Hone, "Boron nitride substrates for high-quality graphene electronics," *Nature Nanotechnology* **5**, 722– (2010).
 - ¹⁰ L. Wang, I. Meric, P. Y. Huang, Q. Gao, Y. Gao, H. Tran, T. Taniguchi, K. Watanabe, L. M. Campos, D. A. Muller, J. Guo, P. Kim, J. Hone, K. L. Shepard, and C. R. Dean, "One-dimensional electrical contact to a two-dimensional material," *Science* **342**, 614–617 (2013).
 - ¹¹ J. R. Wallbank, A. A. Patel, M. Mucha-Kruczynski, A. K. Geim, and V. I. Fal'ko, "Generic miniband structure of graphene on a hexagonal substrate," *Phys. Rev. B* **87**, 245408 (2013).
 - ¹² Pilkyung Moon and Mikito Koshino, "Electronic properties of graphene/hexagonal-boron-nitride moiré superlattice," *Phys. Rev. B* **90**, 154406 (2014).
 - ¹³ Carlos Forsythe, Xiaodong Zhou, Kenji Watanabe, Takashi Taniguchi, Abhay Pasupathy, Pilkyung Moon, Mikito Koshino, Philip Kim, and Cory R. Dean, "Band structure engineering of 2d materials using patterned dielectric superlattices," *Nature Nanotechnology* **13**, 566–571 (2018).
 - ¹⁴ Martin Drienovsky, Andreas Sandner, Christian Baumgartner, Ming-Hao Liu, Takashi Taniguchi, Kenji Watanabe, Klaus Richter, Dieter Weiss, and Jonathan Eroms, "Few-layer graphene patterned bottom gates for van der waals heterostructures," (2017), arxiv:1703.05631.
 - ¹⁵ Martin Drienovsky, Jonas Joachimsmeier, Andreas Sandner, Ming-Hao Liu, Takashi Taniguchi, Kenji Watanabe, Klaus Richter, Dieter Weiss, and Jonathan Eroms, "Commensurability oscillations in one-dimensional graphene superlattices," *Phys. Rev. Lett.* **121**, 026806 (2018).
 - ¹⁶ D. J. Thouless, M. Kohmoto, M. P. Nightingale, and M. den Nijs, "Quantized hall conductance in a two-dimensional periodic potential," *Phys. Rev. Lett.* **49**, 405–408 (1982).
 - ¹⁷ Ming-Hao Liu, "Theory of carrier density in multigated doped graphene sheets with quantum correction," *Phys. Rev. B* **87**, 125427 (2013).
 - ¹⁸ A. H. MacDonald, "Landau-level subband structure of electrons on a square lattice," *Phys. Rev. B* **28**, 6713–6717 (1983).
 - ¹⁹ Qian Niu, D. J. Thouless, and Yong-Shi Wu, "Quantized hall conductance as a topological invariant," *Phys. Rev. B* **31**, 3372–3377 (1985).
 - ²⁰ Hideo Aoki and Tsuneya Ando, "Universality of quantum hall effect: Topological invariant and observable," *Phys. Rev. Lett.* **57**, 3093–3096 (1986).
 - ²¹ G. H. Wannier, "A result not dependent on rationality for bloch electrons in a magnetic field," *physica status solidi (b)* **88**, 757–765 (1978).
 - ²² Régis Decker, Yang Wang, Victor W. Brar, William Regan, Hsin-Zon Tsai, Qiong Wu, William Gannett, Alex Zettl, and Michael F. Crommie, "Local electronic properties of graphene on a bn substrate via scanning tunneling microscopy," *Nano Letters* **11**, 2291–2295 (2011).
 - ²³ Matthew Yankowitz, Jiamin Xue, Daniel Cormode, Javier D. Sanchez-Yamagishi, K. Watanabe, T. Taniguchi, Pablo Jarillo-Herrero, Philippe Jacquod, and Brian J. LeRoy, "Emergence of superlattice dirac points in graphene on hexagonal boron nitride," *Nature Physics* **8**, 382– (2012).
 - ²⁴ J Eroms and D Weiss, "Weak localization and transport gap in graphene antidot lattices," *New Journal of Physics* **11**, 095021 (2009).
 - ²⁵ Andreas Sandner, Tobias Preis, Christian Schell, Paula Giudici, Kenji Watanabe, Takashi Taniguchi, Dieter Weiss, and Jonathan Eroms, "Ballistic transport in graphene an-

- tidot lattices,” *Nano Letters* **15**, 8402–8406 (2015).
- ²⁶ Ryuta Yagi, Ryoji Sakakibara, Ryoya Ebisuoka, Jumpei Onishi, Kenji Watanabe, Takashi Taniguchi, and Yasuhiro Iye, “Ballistic transport in graphene antidot lattices,” *Phys. Rev. B* **92**, 195406 (2015).
- ²⁷ Stephen R. Power, Morten Rishøj Thomsen, Antti-Pekka Jauho, and Thomas Garm Pedersen, “Electron trajectories and magnetotransport in nanopatterned graphene under commensurability conditions,” *Phys. Rev. B* **96**, 075425 (2017).
- ²⁸ George Datsaris, Theo Geisel, and Ragnar Fleischmann, “Robustness of ballistic transport in antidot superlattices,” *New Journal of Physics* **21**, 043051 (2019).
- ²⁹ Cheol-Hwan Park, Li Yang, Young-Woo Son, Marvin L. Cohen, and Steven G. Louie, “New generation of massless dirac fermions in graphene under external periodic potentials,” *Phys. Rev. Lett.* **101**, 126804 (2008).
- ³⁰ Bjarke S. Jessen, Lene Gammelgaard, Morten R. Thomsen, David M. A. Mackenzie, Joachim D. Thomsen, José M. Caridad, Emil Duegaard, Kenji Watanabe, Takashi Taniguchi, Timothy J. Booth, Thomas G. Pedersen, Antti-Pekka Jauho, and Peter Bøggild, “Lithographic band structure engineering of graphene,” *Nature Nanotechnology* **14**, 340–346 (2019).
- ³¹ Carlos Forsythe, *Fractal Hofstadter Band Structure in Patterned Dielectric Superlattice Graphene Systems*, Ph.D. thesis, ColumbiaUniversity (2017).
- ³² Ming-Hao Liu, Peter Rickhaus, Péter Makk, Endre Tóvári, Romain Maurand, Fedor Tkatschenko, Markus Weiss, Christian Schönenberger, and Klaus Richter, “Scalable Tight-Binding Model for Graphene,” *Phys. Rev. Lett.* **114**, 036601 (2015).
- ³³ Elliott H. Lieb, “Two theorems on the hubbard model,” *Phys. Rev. Lett.* **62**, 1201–1204 (1989).
- ³⁴ Wun-Hao Kang, Szu-Chao Chen, and Ming-Hao Liu, “Cloning of zero modes in one-dimensional graphene superlattices,” (2019), arxiv:1912:13202.
- ³⁵ Filippo Pizzocchero, Lene Gammelgaard, Bjarke S. Jessen, José M. Caridad, Lei Wang, James Hone, Peter Bøggild, and Timothy J. Booth, “The hot pick-up technique for batch assembly of van der waals heterostructures,” *Nature Communications* **7**, 11894– (2016).
- ³⁶ Supriyo Datta, *Electronic Transport in Mesoscopic Systems* (Cambridge University Press, Cambridge, 1995).
- ³⁷ M. Beconcini, S. Valentini, R. Krishna Kumar, G. H. Auton, A. K. Geim, L. A. Ponomarenko, M. Polini, and F. Taddei, “Scaling approach to tight-binding transport in realistic graphene devices: The case of transverse magnetic focusing,” *Phys. Rev. B* **94**, 115441 (2016).
- ³⁸ Gaetano Calogero, Nick R Papior, Peter Bøggild, and Mads Brandbyge, “Large-scale tight-binding simulations of quantum transport in ballistic graphene,” *Journal of Physics: Condensed Matter* **30**, 364001 (2018).
- ³⁹ Szu-Chao Chen, Rainer Kraft, Romain Danneau, Klaus Richter, and Ming-Hao Liu, “Electrostatic superlattices on scaled graphene lattices,” (2019), arXiv:1907.03288.
- ⁴⁰ Anders Logg, Kent-Andre Mardal, Garth N. Wells, *et al.*, *Automated Solution of Differential Equations by the Finite Element Method* (Springer, 2012).
- ⁴¹ C. Geuzaine and J.-F. Remacle, “Gmsh: a three-dimensional finite element mesh generator with built-in pre- and post-processing facilities,” *International Journal for Numerical Methods in Engineering* **79**, 1309–1331 (2009).

Tunable two-dimensional superlattices in graphene – Supplementary Information

Robin Huber,¹ Ming-Hao Liu,^{2,*} Szu-Chao Chen,² Martin Drienovsky,¹ Andreas Sandner,¹ Kenji Watanabe,³ Takashi Taniguchi,³ Klaus Richter,⁴ Dieter Weiss,¹ and Jonathan Eroms^{1,†}

¹*Institute of Experimental and Applied Physics, University of Regensburg, D-93040 Regensburg, Germany*

²*Department of Physics, National Cheng Kung University, Tainan 70101, Taiwan*

³*National Institute for Materials Science, 1-1 Namiki, Tsukuba 305-0044, Japan*

⁴*Institute of Theoretical Physics, University of Regensburg, D-93040 Regensburg, Germany*

(Dated: February 19, 2020)

I. CALCULATED GATE MAPS OF POLARITY, POTENTIAL STRENGTH AND AVERAGE CHARGE CARRIER DENSITY

Due to the combined action of a backgate and a patterned bottom gate, a tunable superlattice can be induced very efficiently in graphene. This is verified by additional calculations of the polarity regime and potential strength as a function of V_{bg} and V_{pbg} . The polarity map in Fig. S1 a shows regions of unipolar potential modulation (red area for only p-type charge carriers and blue area for only n-type charge carriers) and bipolar potential modulation (white area) calculated by examining the type of charge carriers at positions 1 ($\text{sgn}(n_1)$) and 2 ($\text{sgn}(n_2)$) in the potential landscape induced by the superlattice (see inset of Fig. S1 a). Fig. S1 b shows the corresponding potential strength, i.e. the potential difference $V_1 - V_2$ between positions 1 and 2. The white dashed lines are equipotential lines with corresponding potential strength ranging from zero modulation to several hundred meV modulation amplitude in the bipolar regime. Fig. S1 c shows the calculated average charge carrier density in the system as a function of V_{bg} and V_{pbg} . The black lines show positions of constant average charge carrier density.

II. CALCULATED HIGH RESOLUTION LANDAU FAN DIAGRAM AND TRANSVERSE RESISTANCE R_{xy} AT $B = 200$ MT

Figure S2 shows additional calculated data of longitudinal resistance R_{xx} as a function of patterned bottom gate voltage V_{pbg} and magnetic field B at a backgate voltage of $V_{bg} = 70$ V. The data show pronounced additional features originating at many satellite Dirac points, especially in the bipolar regime. In Fig. S3, the calculated transverse resistance R_{xy} is shown at a magnetic field of $B = 200$ mT in addition to the calculated longitudinal resistance R_{xx} in Fig. 2 a of the main text. Clear sign changes of the Hall resistance R_{xy} at the positions of the satellite Dirac points in R_{xx} can be observed, which is in good agreement to the experimental data shown in Fig. 1 e of the main text.

III. TRANSVERSE CONDUCTANCE G_{xy} IN THE UNIPOLAR REGIME AT $V_{bg} = 70$ V

Fig. S4 shows additional experimental data of G_{xy} in the unipolar regime at $V_{bg} = 70$ V for the same measurement and range of parameters as in Fig. 3 b of the main text. G_{xy} is plotted in units of e^2/h as a function of Landau level filling factor and inverse magnetic flux ϕ_0/ϕ . The dotted circle marks the position where the quantum Hall resistance shows pronounced non-monotonic behaviour approaching the quantum Hall plateau with $\nu = 6$ (see Fig. 3 of the main text).

IV. ADDITIONAL LANDAU FAN DIAGRAMS AT $V_{bg} = 0$ V AND $V_{bg} = 29$ V

The effect of tunable potential modulation becomes also clear by looking at Landau fans at different backgate voltages, i.e. different potential modulation strengths. Figure S5 shows two additional Landau fans at a backgate voltage of $V_{bg} = 0$ V and at $V_{bg} = 29$ V. The longitudinal resistance is plotted as a function of magnetic field and patterned bottom gate voltage. At $V_{bg} = 0$ V mainly the usual quantum Hall effect features are visible, as expected for intrinsic, unmodulated graphene. By increasing the backgate voltage, i.e. increasing the modulation strength, additional minima in R_{xx} start to appear in the bipolar regime due to superlattice induced energy gaps. In the unipolar regime the modulation strength seems to be too weak to have an observable effect and the usual quantum Hall effect for monolayer graphene is visible. At small magnetic fields weak signatures of satellite Dirac peaks can be seen.

V. NON-MONOTONIC HALL CONDUCTIVITY IN THE BIPOLAR REGIME

Figure S6 shows longitudinal conductance and Hall conductivity in the bipolar regime at $V_{bg} = 70$ V and at identical magnetic flux values as in the main part of the paper. Here, at high backgate voltage, i.e., strong potential modulation, many features start to appear. The longitudinal conductance at $\phi_0/\phi = 0.73$ and $\phi_0/\phi = 0.5$ shows many additional minima accompanied by a non-monotonic and strongly fluctuating Hall conductivity.

Again at high magnetic field ($\phi_0/\phi = 0.29$) the usual quantum Hall effect for monolayer graphene is restored. In general the bipolar regime at strong potential modulation shows rich effects which exceed the simple picture

of well separated Landau levels and Hofstadter physics. Due to the high potential strength also Landau level mixing has to be included to give an overall understanding of the observed effects.

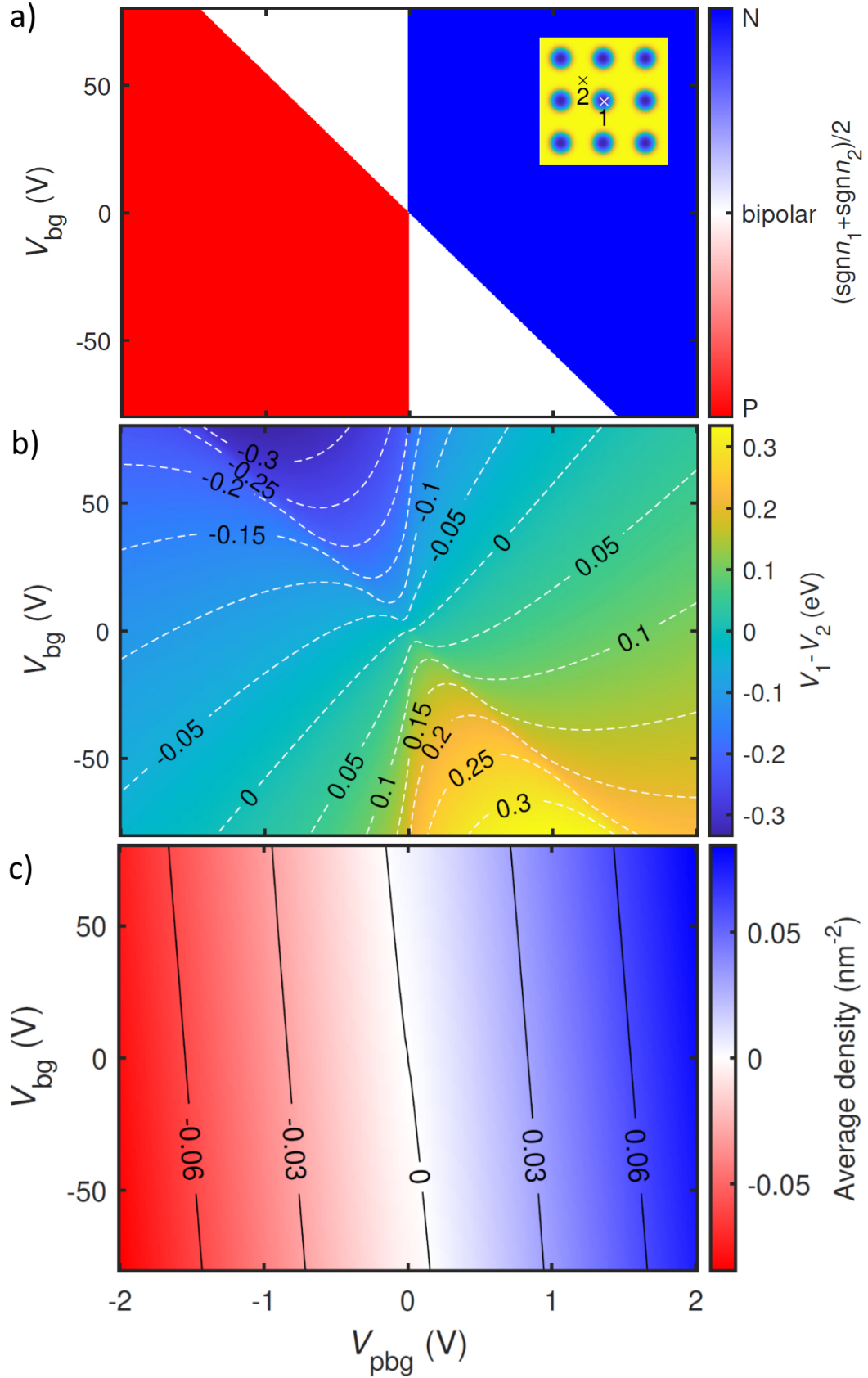


FIG. S1. **Gate maps of polarity, potential strength and average charge carrier density.** a) shows the calculated separation of the gate map into unipolar (red and blue) and bipolar (white) regimes as a function of the applied gate voltages. The potential landscape with positions 1 and 2 is shown in the inset. b) gives information of the calculated potential modulation strengths ranging from zero to several hundred meV modulation amplitude. c) shows the calculated average charge carrier density in the system.

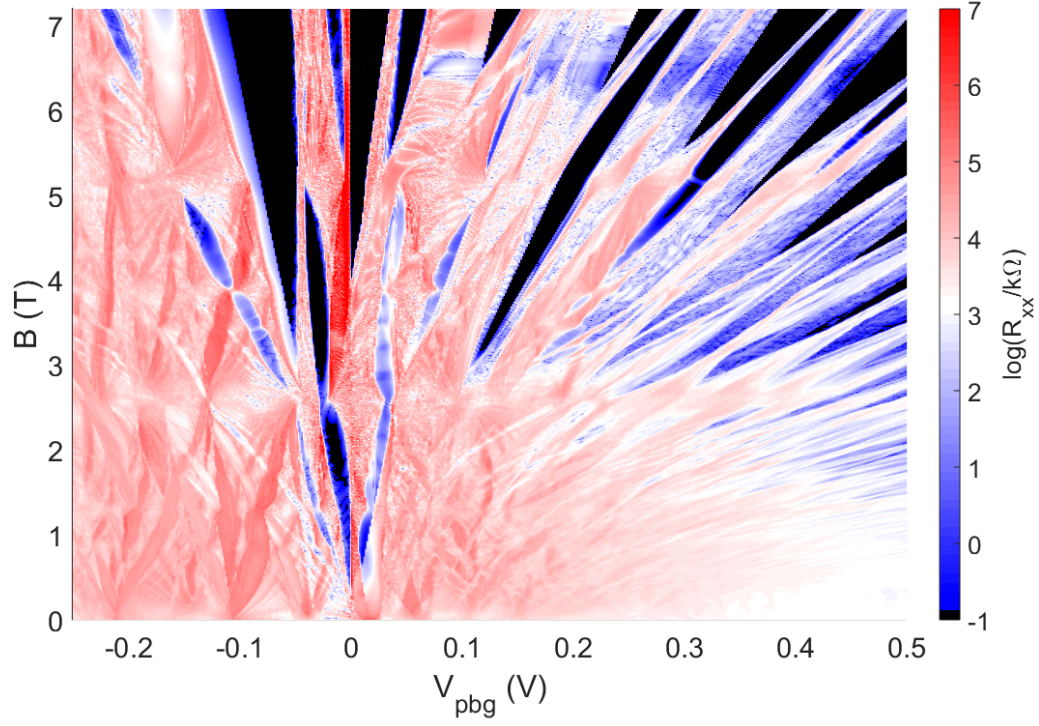


FIG. S2. **Calculated Landau fan diagram** at $V_{bg} = 70$ V. Additional calculated data of longitudinal resistance R_{xx} as a function of patterned bottom gate voltage V_{pbg} and magnetic field B at a backgate voltage of $V_{bg} = 70$ V.

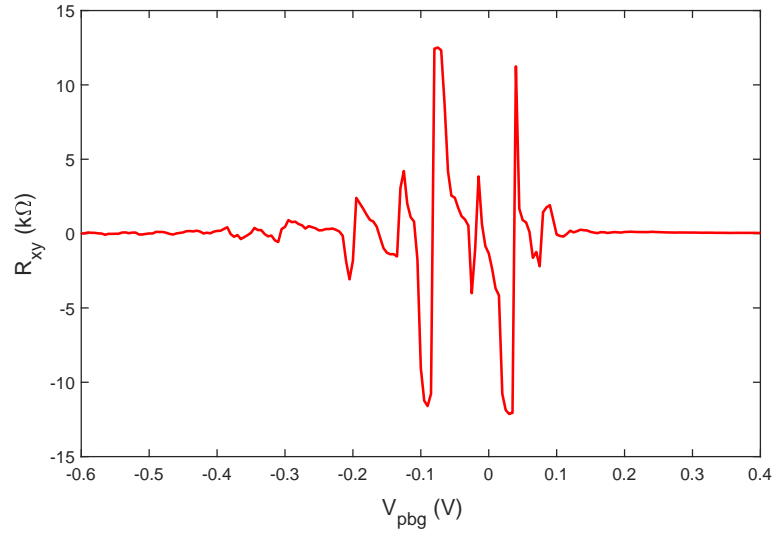


FIG. S3. **Calculated R_{xy}** at $B = 200$ mT. Sign changes of the Hall resistance R_{xy} at the positions of the satellite Dirac points (see Fig. 2 a of the main text) can be observed.

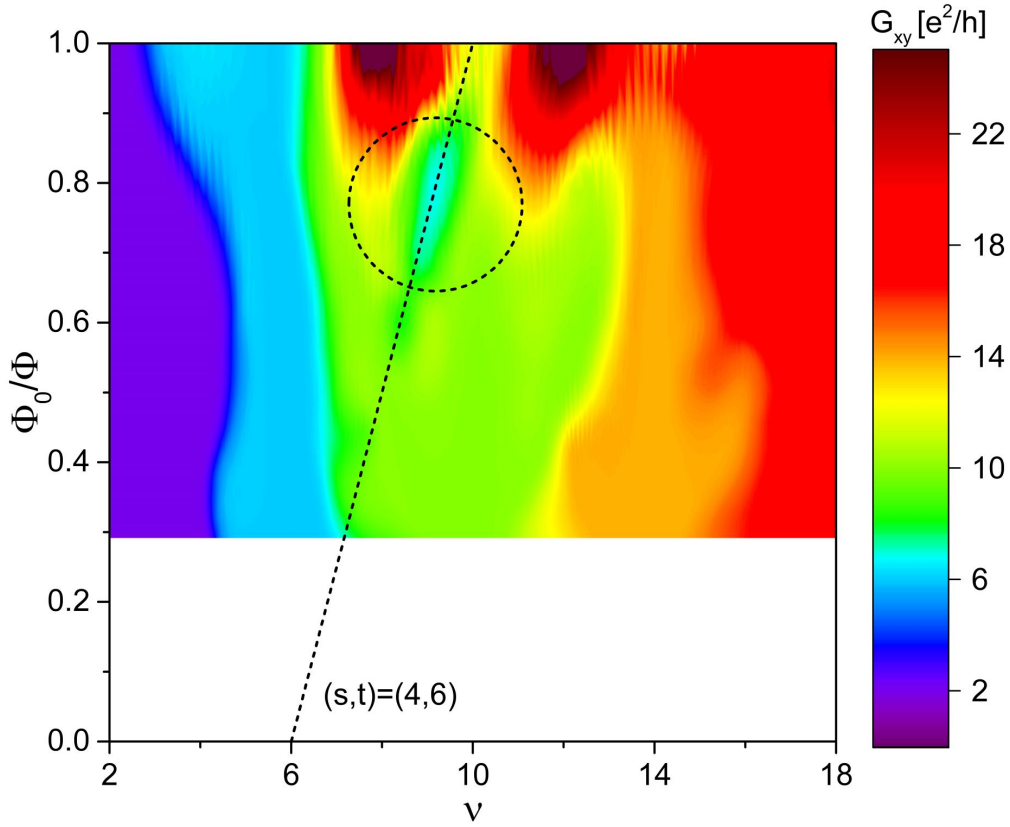


FIG. S4. G_{xy} in units of e^2/h as a function of Landau level filling factor and inverse magnetic flux ϕ_0/ϕ . The dotted circle marks the position of the most pronounced manifestation of a Hofstadter gap with $(s, t) = (4, 6)$ giving rise to the observed non-monotonic quantum Hall resistance.

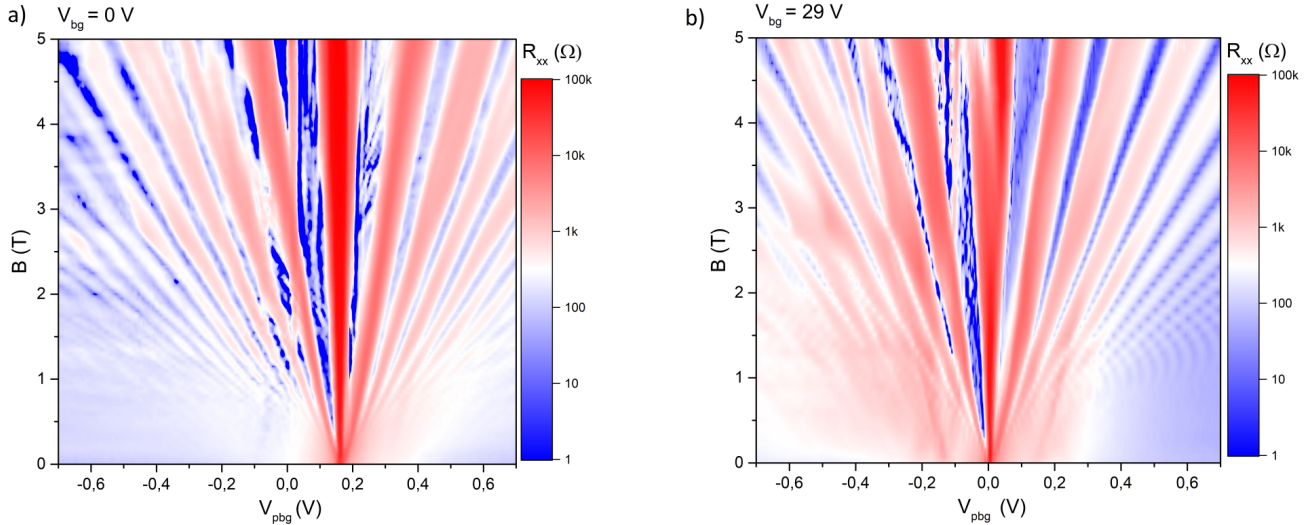


FIG. S5. **a)** Landau fan at a backgate voltage of $V_{bg} = 0$ V. The longitudinal resistance is plotted as a function of magnetic field and patterned bottom gate voltage. At a backgate voltage around $V_{bg} = 0$ V the modulation strength is comparatively small and mainly the usual quantum Hall behaviour of monolayer graphene can be observed. **b)** Landau fan at a backgate voltage of $V_{bg} = 29$ V. At intermediate backgate voltage one can already observe strong effects due to the periodic potential modulation. In the bipolar region the Landau fan diagram shows features corresponding to superlattice induced energy gaps and splitting of Landau levels. In the unipolar regime the potential modulation only has a weak effect on transport and mainly the usual quantum Hall effect in graphene is visible.

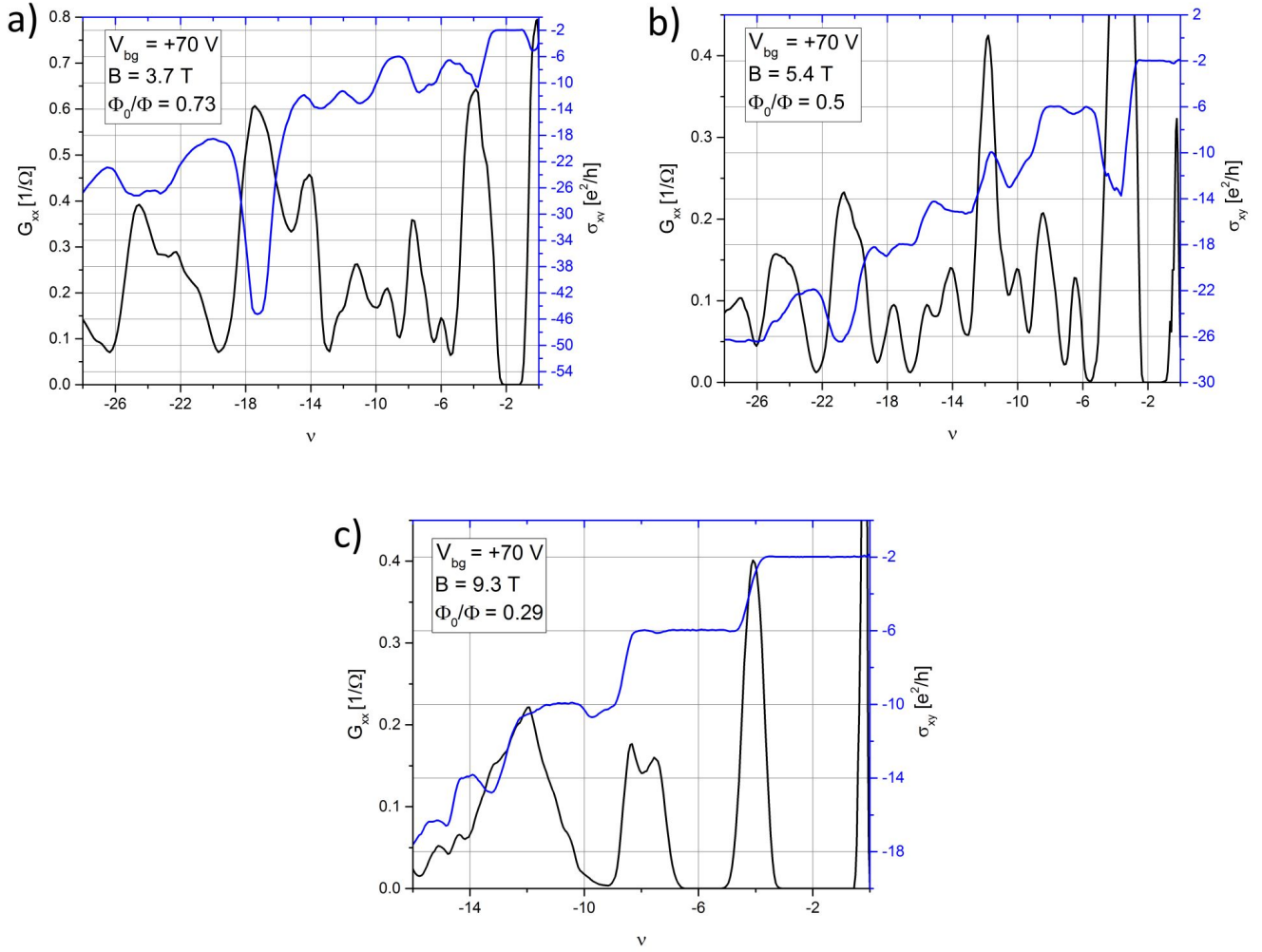


FIG. S6. Measured behaviour of longitudinal conductance and transversal conductivity in the bipolar regime at $V_{bg} = 70$ V at three different values of ϕ_0/ϕ . For a) $\phi_0/\phi = 0.73$ and b) $\phi_0/\phi = 0.5$ the longitudinal conductance shows additional minima in combination with a non-monotonic, fluctuating Hall conductivity. c) At high magnetic field ($\phi_0/\phi = 0.29$) the quantum Hall plateau sequence of monolayer graphene is restored.